Monodisperse SnS$_2$ Nanosheets for High-Performance Photocatalytic Hydrogen Generation

Jing Yu,[†,‡] Cheng-Yan Xu,*[,†,‡] Fei-Xiang Ma,[†,‡] Sheng-Peng Hu,[†,‡] Yu-Wei Zhang,[†,‡] and Liang Zhen*[,†,‡]

[†]School of Materials Science and Engineering, Harbin Institute of Technology, Harbin 150001, People's Republic of China

[‡]MOE Key Laboratory of Micro-systems and Micro-structures Manufacturing, Harbin Institute of Technology, Harbin 150080, People's Republic of China

S *Supporting Information*

ABSTRACT: Graphene-like two-dimensional materials have attracted quite a lot of interest because of their sizable band gaps and potential applications. In this work, monodisperse tin disulfide (SnS$_2$) nanosheets were successfully prepared by a simple solvothermal procedure in the presence of polyvinylpyrrolidone (PVP). Large PVP molecules absorbing on (001) facets of SnS$_2$ would inhibit crystal growth along [001] orientation and protect the product from agglomeration. The obtained SnS$_2$ nanosheets have diameters of ca. 0.8−1 μm and thicknesses of ca. 22 nm. Different experiment parameters were carried out to investigate the transformation of phase and morphology. The formation mechanism was proposed according to the time-dependent experiments. SnS$_2$ nanosheets exhibit high photocatalytic H$_2$ evolution activity of 1.06 mmol h^{-1} g^{-1} under simulated sunlight irradiation, much higher than that of SnS$_2$ with different morphologies and P25-TiO$_2$. Moreover, the as-obtained SnS$_2$ nanosheets show excellent photoelectrochemical response performance in visible-light region.

KEYWORDS: *tin disulfide, nanosheets, solvothermal, photocatalytic hydrogen evolution, photoelectrochemical response*
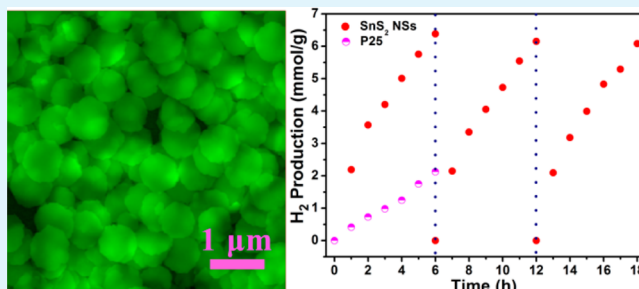
1. INTRODUCTION

Two-dimensional (2D) materials are attracting tremendous attention over the past few years since the isolation of graphene. As is well-known, materials' fundamental properties are closely related to the compositions and arrangement of atoms in themselves. Compared with bulk graphite, 2D graphene exhibits diverse and extraordinary features,[1,2] such as high specific surface area, high Young's modulus, and outstanding thermal and electronic conductivity, resulting in a wide range of potential applications, including energy conversion and storage,[3,4] sensors,[5] electronic and optical devices,[6] and various hybrid materials.[7] Nevertheless, the disadvantage of pristine graphene with zero band gap (E_g) limits its development in field-effect transistors (FETs)[8] and the fabrication of logical circuits.

Recently, graphene analogues, especially metal dichalcogenides, have been widely studied because of their sizable band gap and natural abundance.[9,10] As an important IV−VI semiconductor, tin disulfide (SnS$_2$) with band gap of 2.18−2.44 eV is well-known owing to strong anisotropy of optical properties and interesting applications in gas sensing, FETs, photocatalysis, solar cell, and anode materials.[11−15] SnS$_2$ is an n-type semiconductor with a layered cadmium iodide (CdI$_2$) structure. Tin atom is sandwiched between two close-packed sulfur atoms, forming hexagonal stacking.[16] SnS$_2$ with various morphologies, such as nanowires, nanorods, nanoplates, and nanoflowers have been prepared by bottom-up or top-down

approaches.[17−20] Lotsch et al.[21] reported a facile wet chemistry process toward unilamellar SnS$_2$ nanosheets (NSs) by the exfoliation of Li$_{4x}$Sn$_{1−x}$S$_2$ solid solutions. Tin disulfide single crystals[14] were grown by chemical vapor transport method to fabricate high-performance top-gated field-effect transistors with carrier mobility of 50 cm^2 V^{-1} s^{-1}. Large-scale ultrathin hexagonal tin disulfide NSs[22] were synthesized through a simple hydrothermal process, and employed as high-performance anode materials for Li-ion batteries with 96% capacity retention after 50 cycles. More importantly, SnS$_2$ nanomaterials have good stability in neutral and even acid solutions as well as certain thermal and oxidative stability in atmosphere,[23] which endows it the potential as an outstanding visible-light-sensitive photocatalyst.[24,25] In^{3+}-doped SnS$_2$ hierarchical structures[26] exhibited enhanced photocatalytic activity to three different dyes, methylene blue, methylene green, and ethyl violet. The introduced dopant ion would generate numerous holes which could efficiently suppress the photocorrosion of sulfide photocatalysts. Moreover, the large value of surface to volume ratio can provide more active surface sites. Nevertheless, it is quite indispensable and challenging to explore the possibility of using SnS$_2$ nanomaterials for photocatalytic water splitting. Xie et al.[27] prepared tin disulfide single-layers through the reflux of

bulk SnS_2 to realize efficient photoelectrochemical (PEC) water splitting under visible light. However, there are only a few literature reports[28] regarding photochemical water splitting using SnS_2 as catalyst. In this work, we discuss the feasibility of photochemical water splitting on SnS_2 NSs with indispensable sacrificial reagent.

Herein, we present a simple, one-step solvothermal procedure to prepare SnS_2 nanosheets using polyvinylpyrrolidone (PVP) as surfactant. The reaction time or dosage of PVP has a critical effect on phase and morphology of the products, and the formation mechanism was proposed according to the time-dependent experiments. The obtained SnS_2 NSs exhibit efficient hydrogen evolution capacity under simulated sunlight. The photoelectrochemical property was employed to study the separation and transmission efficiency of photogenerated electrons and holes under visible light ($\lambda > 420$ nm).

2. EXPERIMENTAL SECTION

2.1. Synthesis of Tin Disulfide Nanosheets (SnS_2 NSs). All materials were used as received without further purification. Tin(II) chloride dihydrate ($SnCl_2 \cdot 2H_2O$, 98.0%), thioacetamide (TAA, C_2H_5NS, 99.0%) and triethylene glycol (TEG, $C_6H_{14}O_4$, 98.0%) were purchased from Sinopharm Chemical Reagent Co., Ltd. Polyvinylpyrrolidone ($M_w = 55\,000$) was obtained from Sigma-Aldrich. In a typical synthesis procedure, 1 mmol $SnCl_2 \cdot 2H_2O$, 2 mmol TAA and 0.5 g PVP were added into 30 mL TEG with vigorous magnetic stirring at room temperature. Then the clear solution was transferred into a 50 mL Teflon-lined stainless steel autoclave, heated at 220 °C for 12 h, and cooled to room temperature naturally. The resultant product was centrifuged at 10 000 rpm for 8 min and washed several times with ethanol. Finally, the yellow SnS_2 powder was obtained after dried at 60 °C overnight. In order to investigate the effects of different reaction time or PVP dosage, comparative experiments were carried out by changing single experimental parameter.

2.2. Sample Characterization. Powder X-ray diffraction (XRD) was recorded by Rigaku D/max-IIIB diffractometer with Cu Kα irradiation ($\lambda = 1.541\,78$ Å). The morphologies of the as-synthesized samples were examined by a field-emission scanning electron microscope (SEM, FEI Quanta 200F) and a transmission electron microscope (TEM, JEOL JEM-2100). High-resolution TEM (HRTEM) and selected area electron diffraction (SAED) were also recorded on JEOL JEM-2100 TEM. Energy-dispersive spectroscopy (EDS) measurement was also carried out on FEI Quanta 200F SEM. The thickness of SnS_2 NSs was determined by Bruker Dimension ICON-Pt atomic force microscopy (AFM). UV−vis absorption spectrum was analyzed by using the Shimadzu UV-2550 UV−vis spectrometer. Raman spectrum was measured by a LaBRAM HR800 (Jobin Yvon Horiba) Raman spectrometer with a He—Ne laser (532 nm). X-ray photoelectron spectroscopy (XPS) measurement was conducted on Thermo Fisher Scientific VG Kα Probe spectrometer using Al Kα radiation as the excitation source. Fourier transform infrared (FT-IR) spectroscopy was recorded by Nicolet Avatar 360 FTIR spectrometer.

2.3. Photocatalytic Activity of SnS_2 NSs. Photocatalytic hydrogen evolution from water was carried out in CEL-SPH2N photocatalytic activity evaluation system (Beijing Au-light, China). The reactor used in the photocatalytic process was a cylindrical quartz vessel with height of 10 cm and diameter of 7 cm. The area of the light irradiation is approximately 38.5 cm^2. The system was well sealed with Dow Corning high vacuum grease. A 300W Xe lamp (CEL-HXF 300, Beijing Au-light, China, $I = 20$ A) was employed as simulated sunlight source. In a typical photocatalytic experiment, 20 mg of catalyst powder was dispersed into 100 mL 10 vol % of methanol solution. 0.1 M Na_2S and 0.1 M Na_2SO_3 were added as sacrificial agents. Before catalytic reaction, the whole system was vacuumized using a mechanical pump. Typically, 0.4 mL of gas was extracted each hour and analyzed using online gas chromatograph (GC7890 II,

TECHCOMP, China, N_2 carrier). The amount of hydrogen production was calculated according to the fitted standard curve. The used catalyst was recycled by centrifuging the suspensions after catalytic reaction, and washed with deionized water for several times. The obtained catalyst was then dried in air at 60 °C before the next cycle of reaction.

2.4. Photoelectrochemical Measurements. The photoelectrochemical (PEC) properties of the samples were performed in a conventional three-electrode using an electrochemical workstation (CHI 660E, Chenhua, China). A Pt wire and saturated calomel electrode (SCE) were used as the counter and reference electrodes. The work electrode was prepared by depositing 1 mL 1.5 mg mL^{-1} of sample on the 1×1 cm^2 indium tin oxide (ITO)-coated glass. Subsequently, the ITO glass was heated at 60 °C for 1 h to volatilize the solvent and steady the sample. The electrolyte was composed of 0.5 M Na_2SO_4 aqueous solution (pH = 6). A 300W Xe lamp (CEL-HXF 300, Beijing Au-light, China, $I = 20$ A) with 420 nm cutoff filter was employed as incident light source to study the PEC response of the samples. The electrochemical impedance spectroscopy (EIS) was performed at a bias potential of 0.8 V vs SCE with a frequency of 100 kHz−100 mHz.

3. RESULTS AND DISCUSSION

3.1. Characterization of SnS_2 NSs. The crystal structure and phase composition of the as-prepared SnS_2 NSs were examined by XRD. As shown in Figure 1, all the XRD peaks
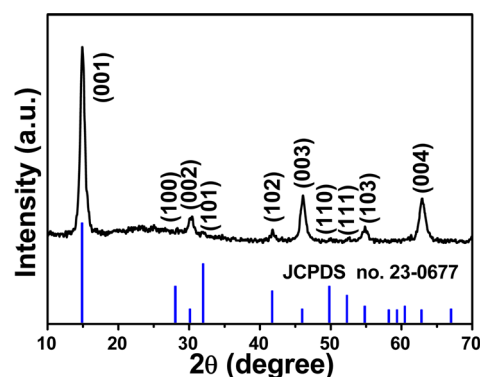

Figure 1. XRD pattern of SnS_2 NSs prepared at 220 °C for 12 h. The lower panel show standard diffraction patterns from SnS_2.

can be readily indexed to the standard diffraction data of JCPDS no. 23-0677, representing 2T-type hexagonal SnS_2 (space group $P\bar{3}m1$) with cell parameters of $a = b = 3.649$ Å and $c = 5.899$ Å. The strong reflections and no impurity peaks demonstrated a high crystallinity and purity of the product. The strongest peak could be assigned to the (001) facet of hexagonal SnS_2, and the diffraction peaks of (002), (003), and (004) facets hold quite strong intensity compared with standard value. This reasonably demonstrates that (001) orientation is preferentially oriented. Furthermore, exposed (001) facets make thin nanosheets preferentially lie on the substrate, forming (001)-oriented films.

Figure 2a,b shows the typical SEM images of SnS_2 NSs. The low-magnification SEM image in Figure 2a presents large-scale 2D nanosheets with good distribution and uniform dimension. High-magnification SEM image (Figure 2b) clearly exhibits regular sheet-like morphology with smooth surface. Supporting Information (SI) Figure S1 provides the EDS analysis spectrum of SnS_2 NSs. The atomic ratio of Sn/S was calculated to be 1:1.9, close to stoichiometric SnS_2 compound. Elemental distribution analysis was also carried out by EDS elemental
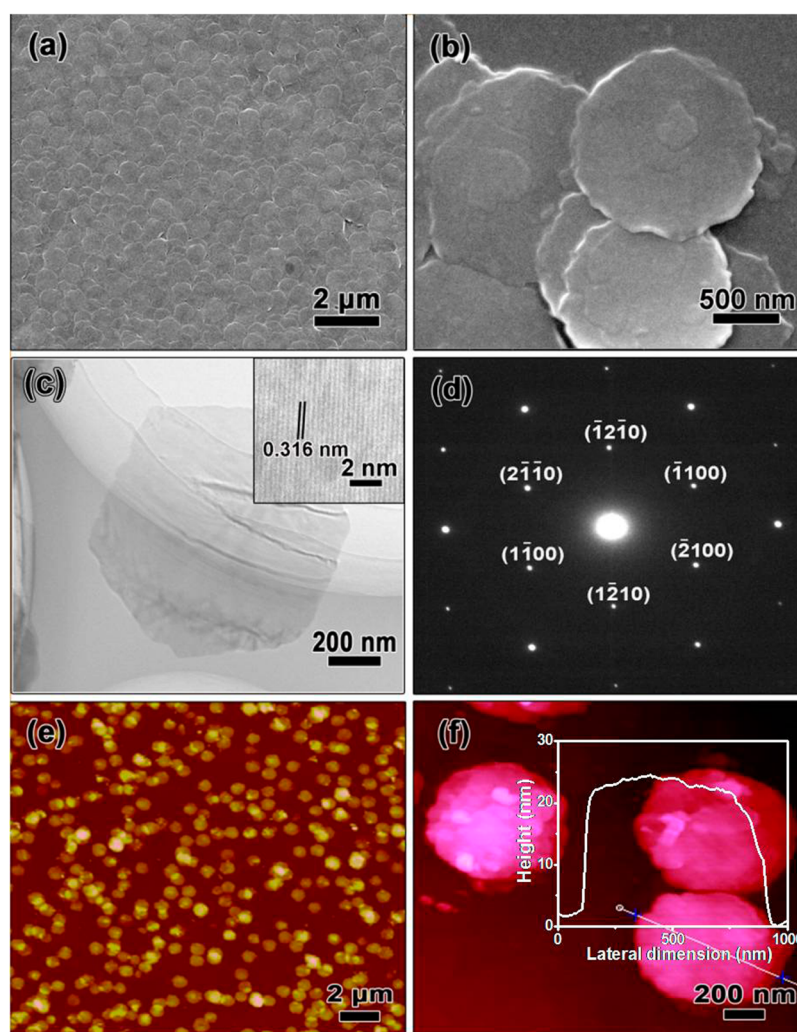
Figure 2. Characterization of SnS_2 nanosheets. (a, b) Typical SEM images with different magnifications. (c) TEM image of an individual nanosheet. Inset is HRTEM image. (d) SAED pattern. (e) Low-magnification AFM image. (f) High-magnification AFM image and corresponding height profile.

mapping, which clearly confirms a well-defined compositional profile of Sn and S elements. In order to further investigate the intrinsic morphology and structure features of SnS_2 NSs, TEM, HRTEM, and SAED were performed, as shown in Figure 2c,d. TEM image in Figure 2c illustrates typical sheet-like structure with quasi-hexagonal stacking. The lattice fringes with lattice spacing of 0.316 nm (insert in Figure 2c) can be attributed to the $(2\bar{1}\bar{1}0)$ interplane distance of hexagonal $2T$-SnS_2. In addition, the corresponding SAED is presented in Figure 2d. On the basis of the analysis results from different crystallographic orientations, we can reasonably conclude that the obtained SnS_2 NSs are single crystalline and own 2D layered structure with hexagonal symmetry. The thickness of nanosheets can be verified by atomic force microscope. AFM image and corresponding height profile are presented in Figure 2e,f. From Figure 2e, we could observe well-distributed and smooth sheet structures, which are in line with aforementioned SEM and TEM analysis. Furthermore, the height profile displays large and homogeneous 2D sheets with diameters of 0.8−1 μm and a thickness of about 22 nm. The nanosheets are assembled by ca. 35−38 hexagonal SnS_2 layers (the experimental value of single-layer SnS_2 is determined to be 0.61 nm[27]). van der Waals interactions drive each single layer stacking together along the

[001] orientation. Nevertheless, Sn and S atoms are combined through intensively chemical bonds in independent monolayer.

Raman spectroscopy shown in SI Figure S3 gives additional evidence of the chemical compositions of the sample. The Raman band at 313.4 cm^{-1} is assigned to A_{1g} mode of hexagonal SnS_2 according to the group theory analysis conducted in literatures.[29,30] In normal SnS_2 Raman spectrum,[27] the weak intralayer E_g mode should be observed at 200−205 cm^{-1}, however, it was not detected in this report. The absence of E_g mode might be led due to quite weak rejection from Rayleigh scattered radiation detected by the Raman sensor or the selection strategy for scattering geometry.[14] In addition, the FT-IR spectra (SI Figure S4) indicate that only a small amount of organics were remained on the surface of SnS_2 nanosheets.

XPS spectrum in Figure 3a reveals the as-synthesized SnS_2 NSs consisted of Sn and S elements, moreover, no obvious evidence demonstrates the presence of impurities. High-resolution XPS of Sn 3d and S 2p spectra are shown in Figure 3b,c. The evolution of Sn 3d with two strong peaks is observed at 486.2 and 494.6 eV, which were attributed to Sn $3d_{5/2}$ and Sn $3d_{3/2}$, respectively. The high-resolution S 2p core level analysis at binding energies of 161.1 and 162.5 eV correspond to S $2p_{3/2}$
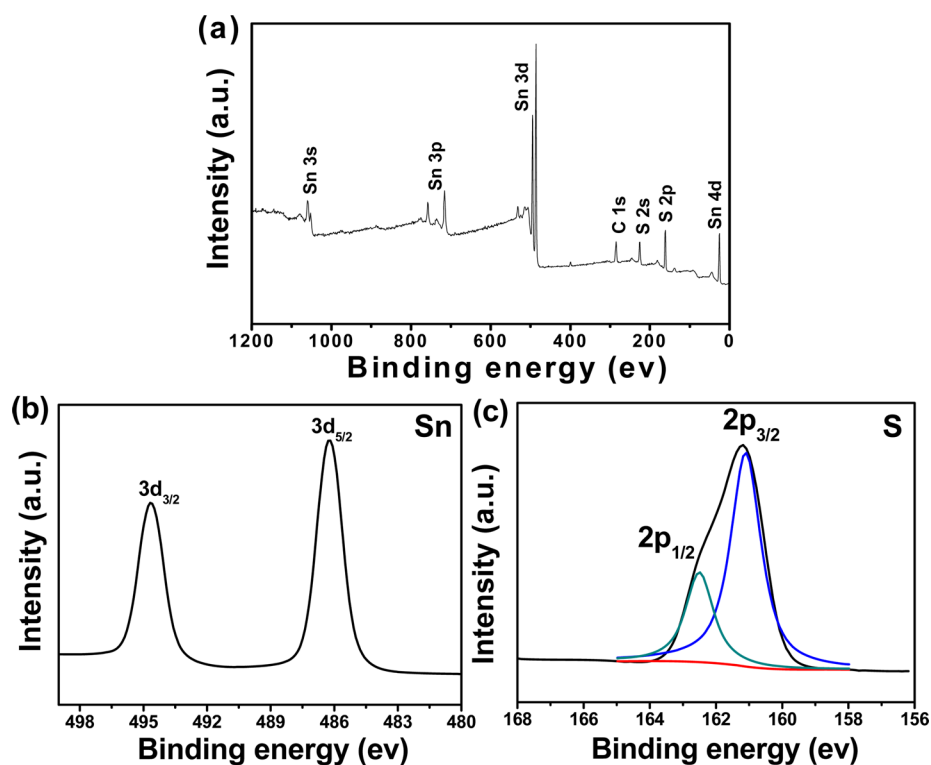
Figure 3. (a) XPS survey spectrum for SnS$_2$ NSs. High-resolution XPS of Sn 3d (b) and S 2p (c) spectra.
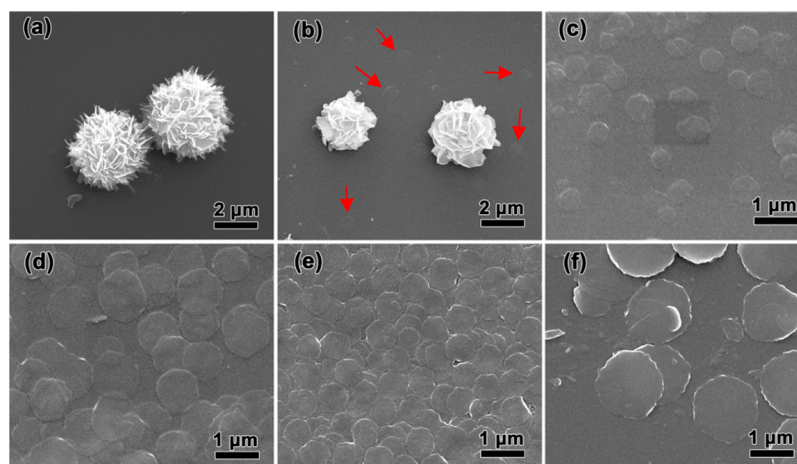

Figure 4. Typical SEM images of the samples prepared at different reaction time. (a) 1 h; (b, c) 2 h; (d) 5 h; (e) 12 h; and (f) 24 h.

and S 2p$_{1/2}$.[31] The observed binding energies of Sn 3d and S 2p spectra are in good accordance with Sn^{4+} and S^{2-} of SnS$_2$.

3.2. Influence of the Reaction Parameters on the Phase and Morphology of the Products. In order to reveal the growth mechanism of SnS$_2$ NSs, it is necessary to understand the phase and morphology transformation of the intermediates during the formation process. Consequently, the effects of reaction parameters, including reaction time or PVP dosage, were investigated by keeping other conditions identical to the typical procedure. PVP has been widely studied as an additive in solution phase synthesis of colloidal particles.[32] As a steric stabilizer or capping agent, the major role of PVP is to protect the product from aggregation and keep good dispersity.[33] In this work, the amount of PVP has also an important effect on the formation of SnS$_2$ NSs. As shown in SI Figure S5, disorderly small plate-like particles were obtained

without PVP added. With the increase of PVP dosage, the samples would change into homogeneous nanosheets from irregular plate-like structure. Besides, the sample exhibits good dispersity when redistributed in ethanol. The colloidal dispersion obtained with 0.5 g PVP is highly stable over 3 days' standing (SI Figure S5f). The corresponding XRD patterns of the products were provided in SI Figure S6. The strongest diffraction peak of the sample without PVP added is attributed to (101) facet, however, (001) orientation would be preferred when lots of PVP molecules were introduced. Therefore, we believe PVP played a vital role in the shaping of 2D crystals. Large PVP molecules would preferentially absorb on the (001) facet of SnS$_2$ nuclei, promoting crystal growth along certain direction,[34] meanwhile, preventing them stacking along the c-axis.[32,35]

The possible formation mechanism was discussed according to the time-dependent experiments. SEM images and corresponding XRD patterns of the as-synthesized products at different reaction durations are given in Figure 4 and SI Figure S7, respectively. In the primary stage of chemical reaction, orthorhombic SnS microspheres stacked by sheets were first nucleated (Figure 4a and SI Figure S7a). With the increase of reaction time to 2 h, small sheets would be expanded and grow into larger sheets. At the same time, the spherical flower-like morphology still remained. Interestingly, regular nanosheets deposited around microflowers could be observed (arrows in Figure 4b). The high-magnification SEM image in Figure 4c clearly exhibits these deposited nanosheets. From the XRD pattern in SI Figure S7b, we can discover the characteristic diffraction peaks of hexagonal SnS_2 besides SnS phase. When the solvothermal process was further prolonged to 5 h, uniform nanosheets were obtained. The corresponding XRD analysis exhibits the single phase of hexagonal SnS_2. Consequently, it can be proved that SnS phase would be oxidized into SnS_2 gradually along with the reaction progress. Furthermore, SnS_2 nanosheets tend to grow up with the reaction time further prolonged. As shown in SI Figure S7c—e, the crystallinity of SnS_2 NSs would be enhanced with extended time, indicating the increased crystal size.

On the basis of the aforementioned analysis results, the possible growth mechanism of SnS_2 NSs is proposed (shown in Scheme 1). The crystal growth habits and environmental

Scheme 1. Possible Formation Mechanism of SnS_2 NSs
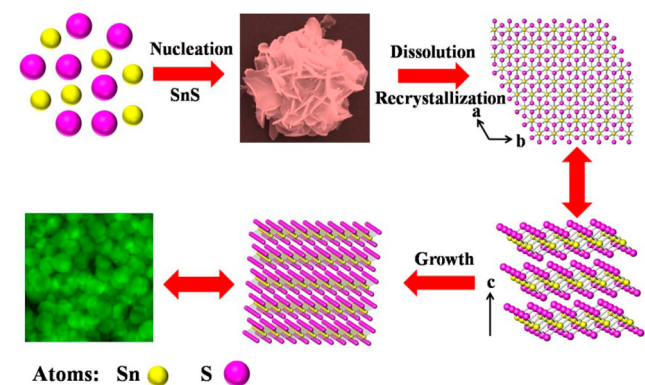
conditions play a significant role in the process of crystal growth.[36] In the first stage, TAA began to decompose and

generated S^{2-} during solvothermal treatment. And then, a rapid nucleation process occurred, where Sn^{2+} from $SnCl_2$ would combine with S^{2-} to form orthorhombic SnS microflowers stacked by decentralized sheets. These narrow sheets would grow along horizontal direction. Because of excess S source added, SnS_2 nuclei would be formed with the increase of reaction time, which might undergo a dissolution-recrystallization growth behavior. During this process, the dissolution of SnS microflowers and the nucleation of hexagonal SnS_2 occurred simultaneously (shown in Figure 4b). SnS_2 nuclei attached along the [001] axis by the driving force from the growth habit of hexagonal SnS_2 crystal. The surface energies of side edges are higher than the surface of nanosheets, therefore, a new layer would be formed on the surface.[37] However, the (001) plane owns the highest reticular densities, which could provide a smaller interatomic distance and larger binding force. Hence, atoms would be more easily adsorbed on the (001) facet for growth.[37] The exposed (001) plane was beneficial to the formation of nanosheets structure. PVP molecules absorbed on the (001) facets would inhibit crystal growth along the [001] orientation. The obtained SnS_2 presents regular and homogeneous sheet structure. After a long time of reaction, SnS_2 NSs tended to grow larger to minimize the surface energy of SnS_2. Finally, SnS_2 nanosheets were fabricated, undergoing the process of nucleation—dissolution—recrystallization—growth.

3.3. Photocatalytic Activity. Generally, the photocatalytic property of a semiconductor is mainly dependent on the photoabsorption ability to available light energy, and the separation and transmission rate of photogenerated electrons and holes in itself. The UV—vis diffuse reflection spectrum was performed to determine the optical absorption of SnS_2 NSs. As shown in SI Figure S8, SnS_2 NSs present strong photoabsorption from UV to the visible light region lower than 580 nm. The intense adsorption band of SnS_2 NSs in the visible light region provides a possibility of excellent visible-light-responsive photocatalysis. The steep edge of the spectrum exposes the visible-light absorption band of SnS_2 is not assigned to the transformation of foreign matter levels but to the band gap transition.[31,38] The band gap energy of semiconductor can be estimated from the UV—visible diffuse reflection spectrum by the following formula:[24] $\alpha h\nu = A(h\nu - E_g)^{n/2}$, where α, h, ν, A, and E_g represent absorption coefficient, Planck constant, light frequency, a constant and optical band gap energy, respectively. Among them, the value of n depends on direct transition ($n = 1$) or indirect transition ($n = 4$) of a
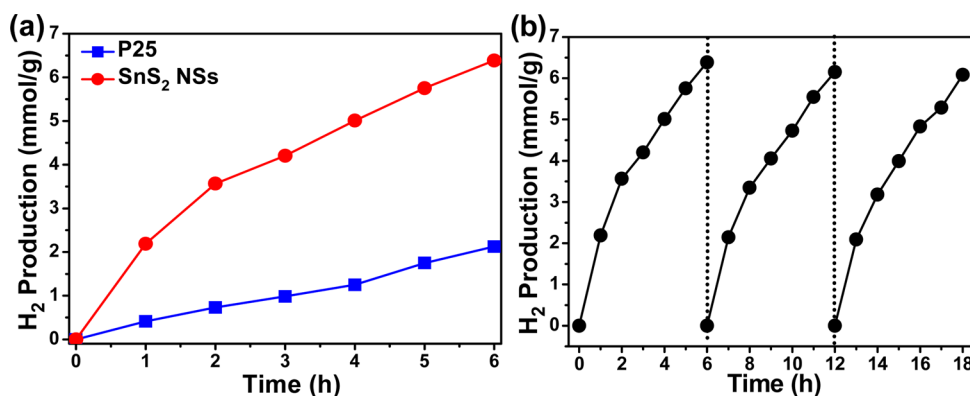

Figure 5. (a) Comparison of the H_2 production rate on commercial $P25$-TiO_2 and SnS_2 NSs. (b) Cyclic H_2 production curve for SnS_2 NSs.
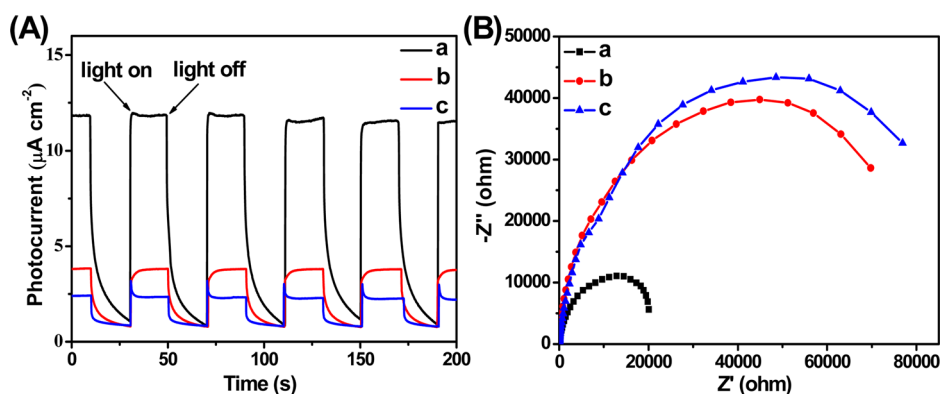
Figure 6. (A) The photoelectrochemical response of the samples at 0.8 V versus SCE electrode under 300 W Xe lamp illumination ($\lambda > 420$ nm). (B) The electrochemical impedance spectra. Z' and Z'' represent the real and imaginary parts of the impedance, while the solid lines were fitted by ZSimpWin software by the equivalent circuits. (a) SnS_2 NSs; (b) the sample obtained without PVP added; and (c) the sample prepared using H_2O as solvent with 0.5 g PVP.

semiconductor. The E_g value of SnS_2 NSs is calculated to be 2.08 eV from the plot $(\alpha h\nu)^2$ versus $h\nu$ (insert in SI Figure S8), which produces a slight red shift phenomenon because of large SnS_2 particles to show quantum confinement related effects.[28] The narrow band gap exhibits its capability of photocatalytic activity driven by visible light.[12]

Recently, chalcogenide nanomaterials have been widely employed toward photochemical hydrogen evolution reaction because of high catalytic activity.[39−41] In this work, photocatalytic H_2 production from water was evaluated using a 300 W xenon lamp to simulate solar irradiation. Na_2S and Na_2SO_3 were used as sacrificial agents to consume photogenerated holes on the surface of catalyst. In general, the VB electrons ($e^−$) of SnS_2 would be excited to CB and create holes (h^+) after absorbing photon energy. The large 2D structure and thin thickness would provide more active sites, and a short and convenient approach where photogenerated electrons and holes migrate to reaction sites of the surface. That can decrease the recombination probability[42] and enhance photocatalytic efficiency. The as-prepared SnS_2 NSs exhibit high activity to hydrogen generation under UV−vis light illumination, and the average H_2 production rate is up to 1.06 mmol h^{-1} g^{-1}, which is higher than previous works (104.9 μmol h^{-1} g^{-1} for $ZnS:Ag_2S$ nanosheets[41] and 838 μmol h^{-1} g^{-1} for $ZnS—CuS—CdS$[43]). Figure 5a shows the comparison of photocatalytic water splitting ability regarding to SnS_2 NSs and commercial P25-TiO_2. The hydrogen evolution capacity of P25-TiO_2 was determined to be 0.35 mmol h^{-1} g^{-1}, which is 2 times less than that of the synthesized SnS_2 NSs. Meanwhile, the photocatalytic activity of SnS_2 spheres and nanoplates were also meausred. SI Figure S10 shows the comparison of H_2-production rate of SnS_2 NSs, spheres, nanoplates, and P25-TiO_2. Obviously, SnS_2 NSs exhibit the highest photocatalytic hydrogen generation ability. The better photocatalytic activity of SnS_2 NSs may be attributed to narrower optical band gap and unique 2D morphology. The cyclic stability of catalytic reaction with 3 periods is shown in Figure 5b. The catalytic activity of SnS_2 NSs did not present any significant loss in the second and third cycles, indicating their suitability and sustainability as photocatalytic hydrogen evolution materials. However, the catalytic activity of SnS_2 nanosheets would decrease with the increasing reaction time in each cycle, which might be attributed to the deactivation of the photocatalyst[44] or the consumption of the sacrificial reagents in the reaction process.[45]

3.4. Photoelectrochemical Performance. In order to further study the separation and transmission efficiency of photogenerated $e^−$ and h^+, the photoelectrochemical property of the synthesized SnS_2 NSs was carried out using photoinduced current−time ($I−t$) curve. The PEC performance of the samples was investigated in 0.5 M Na_2SO_4 electrolyte by a conventional three-electrode system. As shown in Figure 6A, these samples display a quite weak dark current at a bias potential of 0.8 V vs. SCE. However, the as-obtained SnS_2 NSs exhibit a much enhanced photocurrent density of 11.7 μA cm^{-2} under visible light irradiation ($\lambda > 420$ nm). Furthermore, the current would reach steady state with a negligible response time when turning on the light. No apparent photocurrent degradation was observed during repeated ON/OFF switching, clearly revealing the photostability of SnS_2 NSs. In contrast, the $I−t$ curves of irregular SnS_2 nanoplates were also carried out. The photocurrent density was 3.7 μA cm^{-2} and 2.3 μA cm^{-2}, respectively, which are much less than the value of SnS_2 NSs. And the response time is also longer at the moment of the light turning on. The enhanced visible-light response behavior could be attributed to the synergistic effect of macroscopic morphological characteristic and microscopic atomic/electronic structure.[27] The huge contact area and thin thickness enable them to harvest signally increased visible light and help electron−hole pairs to transfer faster, which could reduce the recombination rate of photogenerated electrons and holes. The electrochemical impedance spectra were performed to determine the carrier transport in the electrode. As shown in Figure 6B, SnS_2 NSs exhibit lower interfacial charge-transfer resistance, which would greatly improve carrier transport efficiency. The promotion of conductivity could benefit from homogeneous 2D configuration affording rapid electron transport from the weak conductive SnS_2 nanosheets to the electrode.

4. CONCLUSIONS

The large-size SnS_2 NSs with diameters of 0.8−1 μm and thicknesses of ca. 22 nm were successfully synthesized via a one-step solvothermal method. Experiments of different reaction parameters reveal that orthorhombic SnS microflowers were first formed in the initial step. With the increase of reaction time, SnS would be transferred to be hexagonal SnS_2. As a steric stabilizer or capping agent, PVP molecules would preferentially absorb on the (001) facet of SnS_2 nuclei, inhibit

crystal growth along [001] orientation, and protect the product from aggregation. The as-prepared SnS$_2$ NSs exhibit good dispersity over a long time standing. The formation mechanism was proposed to undergo a nucleation—dissolution—recrystal-lization—growth procedure. SnS$_2$ NSs demonstrate excellent photocatalytic water splitting performance. The average H$_2$ production rate was detected to be 1.06 mmol h^{-1} g^{-1}, which is much higher than that of SnS$_2$ of different morphologies and commercial P25-TiO$_2$. Furthermore, the visible-light response ability is revealed to be outstanding compared with irregular SnS$_2$ nanoplates, indicating the potential application of SnS$_2$ NSs in photodetector and photovoltaic fields. This approach might provide a valuable guidance to the family of MX$_2$ materials.

■ ASSOCIATED CONTENT

ⓢ Supporting Information

EDS, elemental mapping and TEM image of SnS$_2$ nanosheets. Raman and FT-IR spectroscopy for SnS$_2$ nanosheets. SEM images and XRD patterns of the products obtained via adding different amounts of PVP. XRD patterns of the samples prepared for different reaction time. UV—vis diffuse reflection spectrum and plot of $(\alpha h\nu)^2$ vs $h\nu$ for SnS$_2$ nanosheets. SEM images of SnS$_2$ nanoplates and spheres. Comparison of the photocatalytic hydrogen production rate of different samples. This material is available free of charge via the Internet at http://pubs.acs.org.

■ AUTHOR INFORMATION

Corresponding Authors
*E-mail: cy_xu@hit.edu.cn.
*E-mail: lzhen@hit.edu.cn.

Notes
The authors declare no competing financial interest.

■ ACKNOWLEDGMENTS

■ REFERENCES

(1) Novoselov, K. S.; Geim, A. K.; Morozov, S.; Jiang, D.; Zhang, Y.; Dubonos, S.; Grigorieva, I.; Firsov, A. Electric Field Effect in Atomically Thin Carbon Films. *Science* **2004**, *306*, 666−669.

(2) Geim, A. K. Graphene: Status and Prospects. *Science* **2009**, *324*, 1530−1534.

(3) Kim, K. S.; Zhao, Y.; Jang, H.; Lee, S. Y.; Kim, J. M.; Kim, K. S.; Ahn, J.-H.; Kim, P.; Choi, J.-Y.; Hong, B. H. Large-Scale Pattern Growth of Graphene Films for Stretchable Transparent Electrodes. *Nature* **2009**, *457*, 706−710.

(4) Zhu, Y.; Murali, S.; Stoller, M. D.; Ganesh, K.; Cai, W.; Ferreira, P. J.; Pirkle, A.; Wallace, R. M.; Cychosz, K. A.; Thommes, M. Carbon-Based Supercapacitors Produced by Activation of Graphene. *Science* **2011**, *332*, 1537−1541.

(5) Geim, A. K.; Novoselov, K. S. The Rise of Graphene. *Nat. Mater.* **2007**, *6*, 183−191.

(6) Liu, M.; Yin, X.; Ulin-Avila, E.; Geng, B.; Zentgraf, T.; Ju, L.; Wang, F.; Zhang, X. A Graphene-Based Broadband Optical Modulator. *Nature* **2011**, *474*, 64−67.

(7) Yang, X.; Xu, M.; Qiu, W.; Chen, X.; Deng, M.; Zhang, J.; Iwai, H.; Watanabe, E.; Chen, H. Graphene Uniformly Decorated with Gold Nanodots: In Situ Synthesis, Enhanced Dispersibility and Applications. *J. Mater. Chem.* **2011**, *21*, 8096−8103.

(8) Kim, K.; Choi, J.-Y.; Kim, T.; Cho, S.-H.; Chung, H.-J. A Role for Graphene in Silicon-Based Semiconductor Devices. *Nature* **2011**, *479*, 338−344.

(9) Mak, K. F.; Lee, C.; Hone, J.; Shan, J.; Heinz, T. F. Atomically Thin MoS$_2$: A New Direct-Gap Semiconductor. *Phys. Rev. Lett.* **2010**, *105*, 136805.

(10) Splendiani, A.; Sun, L.; Zhang, Y.; Li, T.; Kim, J.; Chim, C.-Y.; Galli, G.; Wang, F. Emerging Photoluminescence in Monolayer MoS$_2$. *Nano Lett.* **2010**, *10*, 1271−1275.

(11) Zhang, Y. C.; Li, J.; Zhang, M.; Dionysiou, D. D. Size-Tunable Hydrothermal Synthesis of SnS$_2$ Nanocrystals with High Performance in Visible Light-Driven Photocatalytic Reduction of Aqueous Cr(VI). *Environ. Sci. Technol.* **2011**, *45*, 9324−9331.

(12) Mondal, C.; Ganguly, M.; Pal, J.; Roy, A.; Jana, J.; Pal, T. Morphology Controlled Synthesis of SnS$_2$ Nanomaterial for Promoting Photocatalytic Reduction of Aqueous Cr(VI) under Visible Light. *Langmuir* **2014**, *30*, 4157−4164.

(13) Du, Y.; Yin, Z.; Rui, X.; Zeng, Z.; Wu, X. J.; Liu, J.; Zhu, Y.; Zhu, J.; Huang, X.; Yan, Q.; Zhang, H. A Facile, Relative Green, and Inexpensive Synthetic Approach Toward Large-Scale Production of SnS$_2$ Nanoplates for High-Performance Lithium-Ion Batteries. *Nanoscale* **2013**, *5*, 1456−1459.

(14) Song, H. S.; Li, S. L.; Gao, L.; Xu, Y.; Ueno, K.; Tang, J.; Cheng, Y. B.; Tsukagoshi, K. High-Performance Top-Gated Monolayer SnS$_2$ Field-Effect Transistors and Their Integrated Logic Circuits. *Nanoscale* **2013**, *5*, 9666−9670.

(15) Xie, X.; Su, D.; Chen, S.; Zhang, J.; Dou, S.; Wang, G. SnS$_2$ Nanoplatelet@Graphene Nanocomposites as High-Capacity Anode Materials for Sodium-Ion Batteries. *Chem.-Asian J.* **2014**, *9*, 1611−1617.

(16) Greenaway, D. L.; Nitsche, R. Preparation and Optical Properties of Group IV—VI$_2$ Chalcogenides Having the CdI$_2$ Structure. *J. Phys. Chem. Solids* **1965**, *26*, 1445−1458.

(17) Yella, A.; Mugnaioli, E.; Panthöfer, M.; Therese, H. A.; Kolb, U.; Tremel, W. Bismuth-Catalyzed Growth of SnS$_2$ Nanotubes and Their Stability. *Angew. Chem., Int. Ed.* **2009**, *48*, 6426−6430.

(18) Jana, M. K.; Rajendra, H. B.; Bhattacharyya, A. J.; Biswas, K. Green Ionothermal Synthesis of Hierarchical Nanostructures of SnS$_2$ and Their Li-Ion Storage Properties. *CrystEngComm* **2014**, *16*, 3994−4000.

(19) Lin, Y. T.; Shi, J. B.; Chen, Y. C.; Chen, C. J.; Wu, P. F. Synthesis and Characterization of Tin Disulfide (SnS$_2$) Nanowires. *Nanoscale Res. Lett.* **2009**, *4*, 694−698.

(20) Seo, J. W.; Jang, J. T.; Park, S. W.; Kim, C.; Park, B.; Cheon, J. Two-Dimensional SnS$_2$ Nanoplates with Extraordinary High Discharge Capacity for Lithium Ion Batteries. *Adv. Mater.* **2008**, *20*, 4269−4273.

(21) Kuhn, A.; Holzmann, T.; Nuss, J.; Lotsch, B. V. A Facile Wet Chemistry Approach towards Unilamellar Tin Sulfide Nanosheets from Li$_{4x}$Sn$_{1-x}$S$_2$ Solid Solutions. *J. Mater. Chem. A* **2014**, *2*, 6100−6106.

(22) Zhai, C.; Du, N.; Yang, H. Z. Large-Scale Synthesis of Ultrathin Hexagonal Tin Disulfide Nanosheets with Highly Reversible Lithium Storage. *Chem. Commun.* **2011**, *47*, 1270−1272.

(23) Zhang, Y. C.; Du, Z. N.; Li, S. Y.; Zhang, M. Novel Synthesis and High Visible Light Photocatalytic Activity of SnS$_2$ Nanoflakes from SnCl$_2$·2H$_2$O and S Powders. *Appl. Catal. B: Environ.* **2010**, *95*, 153−159.

(24) Chen, P.; Su, Y.; Liu, H.; Wang, Y. Interconnected Tin Disulfide Nanosheets Grown on Graphene for Li-Ion Storage and Photocatalytic Applications. *ACS Appl. Mater. Interfaces* **2013**, *5*, 12073−12082.

(25) Zhong, H.; Yang, G.; Song, H.; Liao, Q.; Cui, H.; Shen, P.; Wang, C.-X. Vertically Aligned Graphene-Like SnS$_2$ Ultrathin Nanosheet Arrays: Excellent Energy Storage, Catalysis, Photoconduction, and Field-Emitting Performances. *J. Phys. Chem. C* **2012**, *116*, 9319−9326.

(26) Lei, Y.; Song, S.; Fan, W.; Xing, Y.; Zhang, H. Facile Synthesis and Assemblies of Flowerlike SnS$_2$ and In^{3+}-Doped SnS$_2$: Hierarchical

Structures and Their Enhanced Photocatalytic Property. *J. Phys. Chem. C* **2009**, *113*, 1280−1285.

(27) Sun, Y.; Cheng, H.; Gao, S.; Sun, Z.; Liu, Q.; Liu, Q.; Lei, F.; Yao, T.; He, J.; Wei, S.; Xie, Y. Freestanding Tin Disulfide Single-Layers Realizing Efficient Visible-Light Water Splitting. *Angew. Chem., Int. Ed.* **2012**, *51*, 8727−8731.

(28) Kim, K. M.; Kwak, B. S.; Kang, S.; Kang, M. Synthesis of Submicron Hexagonal Plate-Type SnS_2 and Band Gap-Tuned $Sn_{1-x}Ti_xS_2$ Materials and Their Hydrogen Production Abilities on Methanol/Water Photosplitting. *Int. J. Photoenergy* **2014**, *2014*, Article ID 479508, 9 pages, http://dx.doi.org/10.1155/2014/479508.

(29) Luo, B.; Fang, Y.; Wang, B.; Zhou, J.; Song, H.; Zhi, L. Two Dimensional Graphene-SnS_2 Hybrids with Superior Rate Capability for Lithium Ion Storage. *Energy Environ. Sci.* **2012**, *5*, 5226−5230.

(30) Wang, C.; Tang, K.; Yang, Q.; Qian, Y. Raman Scattering, Far Infrared Spectrum and Photoluminescence of SnS_2 Nanocrystallites. *Chem. Phys. Lett.* **2002**, *357*, 371−375.

(31) Wei, R.; Hu, J.; Zhou, T.; Zhou, X.; Liu, J.; Li, J. Ultrathin SnS_2 Nanosheets with Exposed {001} Facets and Enhanced Photocatalytic Properties. *Acta Mater.* **2014**, *66*, 163−171.

(32) Fang, Z.; Hao, S.; Long, L.; Fang, H.; Qiang, T.; Song, Y. The Enhanced Photoelectrochemical Response of $SnSe_2$ Nanosheets. *CrystEngComm* **2014**, *16*, 2404−2410.

(33) Xiong, Y.; Washio, I.; Chen, J.; Cai, H.; Li, Z.-Y.; Xia, Y. Poly (vinyl pyrrolidone): A Dual Functional Reductant and Stabilizer for the Facile Synthesis of Noble Metal Nanoplates in Aqueous Solutions. *Langmuir* **2006**, *22*, 8563−8570.

(34) Sun, Y.; Mayers, B.; Herricks, T.; Xia, Y. Polyol Synthesis of Uniform Silver Nanowires: A Plausible Growth Mechanism and the Supporting Evidence. *Nano Lett.* **2003**, *3*, 955−960.

(35) Chen, J. S.; Liu, J.; Qiao, S. Z.; Xu, R.; Lou, X. W. Formation of Large 2D Nanosheetsvia PVP-Assisted Assembly of Anatase TiO_2 Nanomosaics. *Chem. Commun.* **2011**, *47*, 10443−10445.

(36) Ma, J.; Wang, Y.; Wang, Y.; Chen, Q.; Lian, J.; Zheng, W. Controlled Synthesis of One-Dimensional Sb_2Se_3 Nanostructures and Their Electrochemical Properties. *J. Phys. Chem. C* **2009**, *113*, 13588−13592.

(37) Feng, J.; Chen, J.; Geng, B.; Feng, H.; Li, H.; Yan, D.; Zhuo, R.; Cheng, S.; Wu, Z.; Yan, P. Two-Dimensional Hexagonal SnS_2 Nanoflakes: Fabrication, Characterization, and Growth Mechanism. *Appl. Phys. A: Mater. Sci. Process.* **2011**, *103*, 413−419.

(38) Tsuji, I.; Kato, H.; Kudo, A. Photocatalytic Hydrogen Evolution on ZnS−$CuInS_2$−$AgInS_2$ Solid Solution Photocatalysts with Wide Visible Light Absorption Bands. *Chem. Mater.* **2006**, *18*, 1969−1975.

(39) Jin, J.; Yu, J.; Liu, G.; Wong, P. K. Single Crystal CdS Nanowires with High Visible-Light Photocatalytic H_2-Production Performance. *J. Mater. Chem. A* **2013**, *1*, 10927−10934.

(40) Pang, H.; Wei, C.; Li, X.; Li, G.; Ma, Y.; Li, S.; Chen, J.; Zhang, J. Microwave-Assisted Synthesis of NiS_2 Nanostructures for Supercapacitors and Cocatalytic Enhancing Photocatalytic H_2 Production. *Sci. Rep.* **2014**, *4*, 3577.

(41) Yang, X.; Xue, H.; Xu, J.; Huang, X.; Zhang, J.; Tang, Y.-B.; Ng, T.-W.; Kwong, H.-L.; Meng, X.-M.; Lee, C.-S. Synthesis of Porous ZnS:Ag_2S Nanosheets by Ion Exchange for Photocatalytic H_2 Generation. *ACS Appl. Mater. Interfaces* **2014**, *6*, 9078−9084.

(42) Kudo, A.; Miseki, Y. Heterogeneous Photocatalyst Materials for Water Splitting. *Chem. Soc. Rev.* **2009**, *38*, 253−278.

(43) Hong, E.; Kim, D.; Kim, J. H. Heterostructured Metal Sulfide (ZnS—CuS—CdS) Photocatalyst for High Electron Utilization in Hydrogen Production from Solar Water Splitting. *J. Ind. Eng. Chem.* **2014**, *20*, 3869−3874.

(44) Bao, N.; Shen, L.; Takata, T.; Domen, K. Self-Templated Synthesis of Nanoporous CdS Nanostructures for Highly Efficient Photocatalytic Hydrogen Production under Visible Light. *Chem. Mater.* **2007**, *20*, 110−117.

(45) Li, Y.; Chen, G.; Zhang, H.; Li, Z.; Sun, J. Electronic Structure and Photocatalytic Properties of $ABi_2Ta_2O_9$ (A = Ca, Sr, Ba). *J. Solid State Chem.* **2008**, *181*, 2653−2659.